The Astrophysical Journal, 665:554–568, 2007 August 10

GRB 060714: NO CLEAR DIVIDING LINE BETWEEN PROMPT EMISSION AND X-RAY FLARES

H. A. Krimm,[1,2] J. Granot,[3] F. E. Marshall,[4] M. Perri,[5] S. D. Barthelmy,[4] D. N. Burrows,[6] N. Gehrels,[4] P. Mészáros,[6] and D. Morris[6]

Received 2007 February 22; accepted 2007 April 20

ABSTRACT

The long gamma-ray burst GRB 060714 was observed to exhibit a series of five X-ray flares beginning ~70 s after the burst trigger T_0 and continuing until $\sim T_0 + 200$ s. The first two flares were detected by the Burst Alert Telescope (BAT) on the *Swift* satellite, before *Swift* had slewed to the burst location, while the last three flares were strongly detected by the X-Ray Telescope (XRT) but only weakly detected by the BAT. This burst provides an unusual opportunity to track a complete sequence of flares over a wide energy range. The flares were very similar in their light curve morphology, showing power-law rise and fall components, and in most cases significant substructure. The flares also showed strong evolution with time, both spectrally and temporally. The small timescale and large amplitude variability observed are incompatible with an external shock origin for the flares, and support instead late-time sporadic activity either of the central source or of localized dissipation events within the outflow. We show that the flares in GRB 060714 cannot be the result of internal shocks in which the contrast in the Lorentz factor of the colliding shells is very small, and that this mechanism faces serious difficulties in most *Swift* GRBs. The morphological similarity of the flares and the prompt emission and the gradual and continual evolution of the flares with time makes it difficult and arbitrary to draw a dividing line between the prompt emission and the flares.

Subject headings: gamma rays: bursts

1. INTRODUCTION

One of the most surprising findings of the studies of gamma-ray bursts (GRBs) made with the *Swift Gamma-Ray Burst Explorer* (Gehrels et al. 2004) is that nearly half of all bursts show flares, or large short-lived increases in emission at times after the initial prompt emission has died away (Burrows et al. 2005b; Nousek et al. 2006; O'Brien et al. 2006). These flares are superimposed on either the rapidly decaying tail of the prompt emission, or the very slowly decaying phase of the early afterglow, and can involve flux increases of as much as 3 orders of magnitude. Some bursts have single flares, although most bursts with flares have multiple flaring episodes. Most flares are at early times, $t \lesssim 10^3$ s, although strong flares can occur as late as $\gtrsim 10^4$ s after the onset of the burst.

The origin of GRB flares is still an open question. Evidence is mounting, however, that the origin of these flares is similar to that of the prompt GRB emission (i.e., either internal shocks or some other well-localized dissipation process within the ultrarelativistic outflow), rather than to that of the afterglow emission (i.e., the external shock going into the ambient medium). This evidence includes the multiplicity of flares; their sharp time structure (rapid rise and decay and subpeak structure within the flares); the large increase in flux during the flare; and the hard to soft spectral evolution of the flares, which is similar to the spectral evolution found in the prompt emission.

In the context of the internal shocks model (Rees & Mészáros 1994), flares may be caused by late-time collisions of shells of relativistic material that are produced by the central engine with varying Lorentz factors. These can occur either by late-time sporadic activity of the central source, or by a small relative velocity between shells that were ejected during the prompt GRB emission (e.g., Burrows et al. 2007).

Very few GRBs have a sequence of multiple flares bright enough to be studied in detail. GRB 060714 (Krimm et al. 2006a) showed a series of five flares starting at ~70 s after the start of the burst. The first three flares were clearly detected by the *Swift* Burst Alert Telescope (BAT; Barthelmy et al. 2005a), and the last three were seen as strong flares by the *Swift* X-Ray Telescope (XRT; Hill et al. 2004; Burrows et al. 2005a) and as weak flares by the BAT. The first two flares occurred while the spacecraft was slewing to or settling at the burst location, so they were not observable by the XRT. This burst provides a rare opportunity to study a rapid sequence of flares across a large energy range. The five flares show evidence of hard to soft spectral evolution as the flares progress and also strong similarities, in particular, sharply resolved temporal features and large flux increases in each flare. We show that these results are inconsistent with an external shock (i.e., afterglow) origin for the flares and suggest instead a late-time and lower energy continuation of the prompt emission, either due to late-time intermittent activity of the central source or via well-localized spasmodic dissipation events within the outflow.

In fact these results suggest that it may no longer be possible to draw a clear distinction between what have traditionally been called the prompt emission and the X-ray flares. Historically, the prompt emission was that detected above ~20 keV and was generally considered to be due to activity of the central engine. X-ray flares are usually detected most strongly at lower energies, so they were considered a completely separate phenomenon. Since we show here that (1) the flares of GRB 060714 are very likely of common origin to the earliest emission from the burst, (2) the flares are detected above 20 keV, and (3) the flares show a gradual and continual evolution linking them to the prompt emission, it is quite reasonable to consider the flares a lower energy continuation of the same phenomenon as the prompt emission. However, to be consistent with earlier work we do use the term "prompt emission" to refer to the emission in the first peak, ~−13 s before to 20 s after

[1] CRESST and NASA Goddard Space Flight Center, Greenbelt, MD 20771.
[2] Universities Space Research Association, 10211 Wincopin Circle, Suite 500, Columbia, MD 21044.
[3] KIPAC, Stanford University, P.O. Box 20450, MS 29, Stanford, CA 94309.
[4] NASA Goddard Space Flight Center, Greenbelt, MD 20771.
[5] ASI Science Data Center, Via Galileo Galilei, I-00044 Frascati, Italy.
[6] Department of Astronomy and Astrophysics, 525 Davey Laboratory, Pennsylvania State University, University Park, PA 16802.

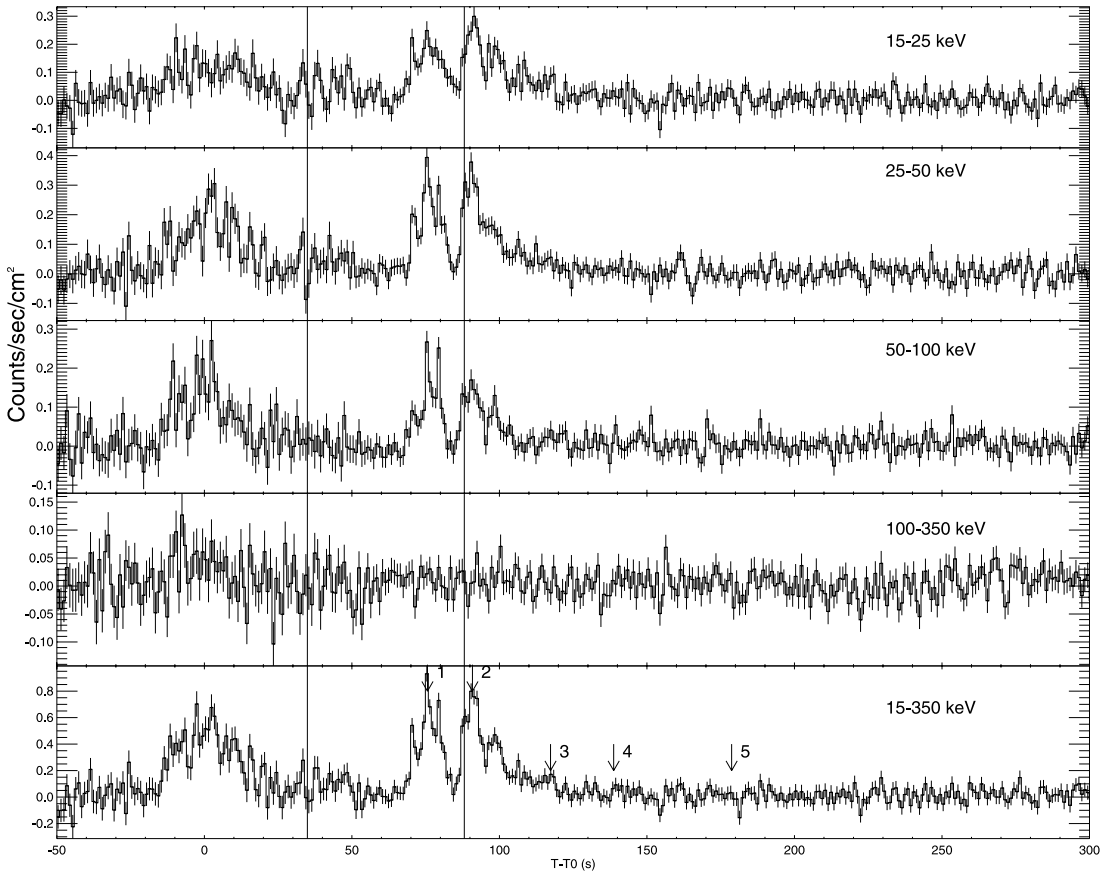

FIG. 1.—BAT light curve in four energy bands and the sum of all energy bands. The vertical bars indicate the start and end of the spacecraft slew to the burst location. Note that the count rate statistical errors are much larger before the slew than after the slew. This is because the burst was detected near the edge of the BAT field of view where only 27% of the detectors were illuminated. None of the apparent sharp structure in the prompt emission is statistically significant. The arrows in the bottom plot indicate the peak and the numbering of each of the flares.

the burst trigger (see § 2.1), "flare" to refer to the peaks more than $\sim$70 s after the trigger, and "afterglow" to refer to the smooth decay $\gtrsim$300 s from the trigger.

In this paper we describe the prompt, flaring, and afterglow properties of GRB 060714, with particular emphasis on the flares. In § 2 we discuss the observations and data analysis in general, while § 3 focuses on the analysis of the spectral and temporal properties of the flares. Finally, in § 4 we show that the properties of the flares rule out an external shock (or long-lived reverse shock) origin and provide some (although not unequivocal) support for an origin common to that of the prompt emission. In § 4.3 and in the Appendix we exclude internal shocks with a small contrast in the Lorentz factor as the origin of the flares in GRB 060714 and point out that this mechanism faces serious problems for most *Swift* GRBs.

Throughout the paper we follow the convention $F_{\nu,t} \propto \nu^{-\beta} t^{-\alpha}$, where the energy spectral index β is related to the photon index $\Gamma = \beta + 1$. We have adopted the standard values of the cosmological parameters: $H_0 = 70$ km s^{-1} Mpc^{-1}, $\Omega_M = 0.27$, and $\Omega_\Lambda = 0.73$. The phenomenology of the burst is presented in the observer frame unless otherwise stated.

2. OBSERVATIONS AND DATA ANALYSIS

2.1. *Swift BAT*

At 15:12:00 UT, 2006 July 14, the *Swift* Burst Alert Telescope (BAT) triggered and located on board GRB 060714 (BAT trigger = 219101; Krimm et al. 2006a). Unless otherwise specified, times t in this paper are measured from the BAT trigger time, (UT 15:12:00.3), hereafter designated T_0. The burst was detected in the part of the BAT field of view that was 27% coded, meaning that it was 33.6° off-axis and only 27% of the BAT detectors were illuminated by the source. The spacecraft began to slew to the source location at $T_0 + 34.9$ s and was settled at the source location at $T_0 + 88.1$ s.

The BAT data for GRB 060714 between $T_0 - 240$ s and +962 s were collected in event mode with 100 μs time resolution and $\sim$6 keV energy resolution (Krimm et al. 2006b). The data were processed using standard *Swift* BAT analysis tools, and the spectra were fit using XSPEC version 11.3. Each BAT event was mask-tagged using `batmaskwtevt` with the best fit source position. Mask tagging is a technique in which each event is weighted by a factor representing the fractional exposure to the source through the BAT coded aperture. A weight of +1 corresponds to a fully open detector and a weight of -1 to a fully blocked detector. Flux from the background and other sources averages to zero with this method. All of the BAT GRB light curves shown in Figures 1 and 2 (see also Fig. 7, below) have been background subtracted by this method. This method is effective even when the spacecraft is moving, since complete aspect information is available during the maneuver.

The mask weighting is also applied to produce weighted, background-subtracted counts spectra using the tool `batbinevt`. Since the response matrix depends on the position of the source in the BAT field of view, separate matrices are derived for before the slew, for after the slew, and for individual segments of the light curve during the slew.

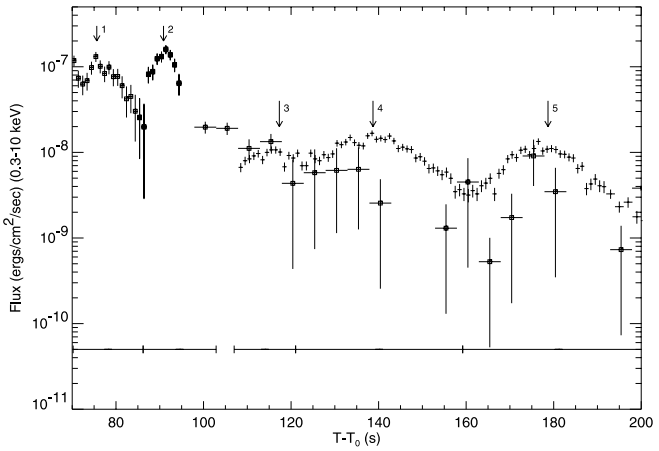

FIG. 2.—Five flares for both BAT (*open squares*) and XRT (*plus signs*). The first XRT flare at $T \sim 115$ s is clearly detected in the BAT, and there appears to BAT emission at the peak of the flare at $T \sim 175$ s. The arrows indicate the peak and the numbering of each of the flares. The time for which the spectral fits to the five flares were made are indicated by the bars at the bottom of the plot.

The mask-weighted light curves seen in Figure 1 show an initial triangular-shaped (rising and falling power laws) peak starting at $T_0 - 15$ s, peaking at T_0, and ending at $T_0 + 55$ s. Given the size of the statistical error bars in the time before the slew, none of the fluctuations seen in Figure 1 before the slew are statistically significant. The initial prompt emission was followed by two strong flares, the first starting at $T_0 + 70.4$ s with a duration of ~10.5 s, and the second starting at $T_0 + 87.6$ s with a duration of ~12 s. Finally there was a much weaker third flare, starting at $T_0 + 108.7$ s with a duration of ~15.3 s. Taking into account the prompt emission plus the flares, we derive $T_{90} = 115 \pm 5$ s (estimated error including systematics).

The time-averaged spectrum from $T_0 - 13.4$ s to +18.0 s is best fit by a simple power-law model. The power-law photon index of the time-averaged spectrum is $\Gamma = -d\log N_{\rm ph}/d\log E_{\rm ph} = 1.61 \pm 0.13$ ($\chi^2 = 43.2$ for 59 degrees of freedom). The fluence in the 15–150 keV band is $(1.22 \pm 0.11) \times 10^{-6}$ erg cm^{-2}. The 1 s peak photon flux measured from $T_0 + 75.42$ s (during the first flare) in the 15–150 keV band is 1.4 ± 0.1 photons cm^{-2} s^{-1}. The prompt component does show spectral evolution, as evidenced by the increasing power-law index: 1.47 ± 0.19 for $T_0 - 13.4$ to +2.1 s, 1.61 ± 0.17 for $T_0 + 2.1$ to +18.0 s, and 2.29 ± 0.49 for $T_0 + 18.0$ to +70.2 s. All the quoted errors are at the 90% confidence level.

We attempted to fit a model consisting of a power law with an exponential cutoff to the prompt emission. Such a fit did not constrain $E_{\rm pk}$, the peak of the $\nu F(\nu)$ spectrum. However, it may be possible to use the results of Zhang et al. (2007) to estimate $E_{\rm pk}$ for the prompt emission. Zhang et al. (2007) have shown that due to the relatively narrow energy band of BAT, it is often difficult to constrain $E_{\rm pk}$, even when $E_{\rm pk}$ is within the BAT energy range. These authors have found that the power-law photon index Γ of a simple power-law fit and $E_{\rm pk}$ are well correlated with a relationship

$$\log E_{\rm pk} = (2.76 \pm 0.07) - (3.61 \pm 0.26) \log \Gamma, \qquad (1)$$

under the assumption that $E_{\rm pk}$ is within the BAT energy range. Sakamoto et al. (2007) have reached a similar conclusion and consistent result by combining simulations and a study of bursts for which $E_{\rm pk}$ has been determined. We can use equation (1) and the measured $\Gamma = 1.61$, to find that $E_{\rm pk} = 103.1^{+34.0}_{-25.5}$ keV. This value of $E_{\rm pk}$ is consistent with the majority of long GRBs detected by BAT. However, another possibility is that $E_{\rm pk}$ is above the BAT energy range (>150 keV), and 1.61 is instead simply the low-energy power-law index α. According to the study of Kaneko et al. (2006) a value of $\alpha = 1.61$ is within the range of α values found for BATSE bursts, although only 22 of the 350 bursts in the BATSE sample (6.3%) have $\alpha > 1.61$. Since we cannot exclude this second possibility, we will be conservative and quote only a lower limit, $E_{\rm pk} > 77.6$ keV (taking the lower limit on $E_{\rm pk}$ as derived from eq. [1]). As discussed in § 3, $E_{\rm pk}$ is well constrained for the later flares.

2.2. *Swift XRT*

The spacecraft slewed immediately to the BAT location of GRB 060714 and the *Swift* X-Ray Telescope (XRT) began observing the burst at 15:13:39 UT ($T_0 + \sim 99$ s), first in Image mode and then in Photodiode (PD) mode. The Image mode contains no spectral or timing information and the PD mode data is severely corrupted by the presence of two hot columns. Thus, the first usable data is in Windowed Timing (WT) mode beginning at $T_0 + 107$ s (see Hill et al. 2004 for a description of XRT readout modes). Starting from $T_0 + 249$ s all observations were carried out in Photon Counting (PC) mode.

The XRT data were processed with the XRTDAS software (ver. 1.7.1) developed at the ASI Science Data Center and included in the HEAsoft package (ver. 6.0.4). Event files were calibrated and cleaned with standard filtering criteria with the `xrtpipeline` task using the latest calibration files available in the *Swift* CALDB distributed by HEASARC. Event lists were selected in the 0.3–10.0 keV energy band and grades 0–12 for PC mode data and grades 0–2 for WT data were used in the analysis (see Burrows et al. 2005a for a definition of XRT event grades).

The XRT PC image of the field clearly showed a bright fading X-ray object in the field (Perri et al. 2006). The coordinates of the burst were determined by the XRT to be (J2000.0) R.A. = $15^{\rm h}11^{\rm m}26.5^{\rm s}$ (227.8604°), decl. = $-6°33'59.3''$ (−6.5665°) with a 90% confidence error circle radius of 3.8″.

Events for temporal and spectral analysis of WT mode data were selected using a 40 pixel wide rectangular region centered on the afterglow. Background events were extracted from a nearby source-free rectangular region with a 40 pixel width. Data in PC mode during the first *Swift* orbit (from $T_0 + 249$ s to +1610 s) were significantly affected by pileup. By comparing the observed point-spread function (PSF) profile with the analytical model (Moretti et al. 2005), we removed pileup effects by excluding events within a 2 pixel radius circle centered on the afterglow position and using an outer radius of 20 pixels. From the second orbit, the afterglow count rate was below the XRT pileup limit and events were extracted using a 10 pixel radius circle. The background for PC mode was estimated from a nearby source-free circular region of radius 50 pixels. Source count rates for temporal analysis were corrected for the fraction of PSF falling outside the event extraction regions and for pixels partially exposed. Ancillary response files for the spectral analysis were generated with the `xrtmkarf` task applying corrections for the PSF losses and pixel exposures. The latest response matrices (ver. 008) available in the *Swift* CALDB were used and source spectra were binned to ensure a minimum of 20 counts per bin.

As discussed in detail in § 3, the XRT light curve (Perri et al. 2006) shown in Figures 2 and 3 (see also Fig. 7, below) displays three flares during the first orbit, peaking at about $T_0 + 115$, 140, and 180 s after the BAT trigger. There is a steep decay after the end of the third XRT flare, with temporal power-law index

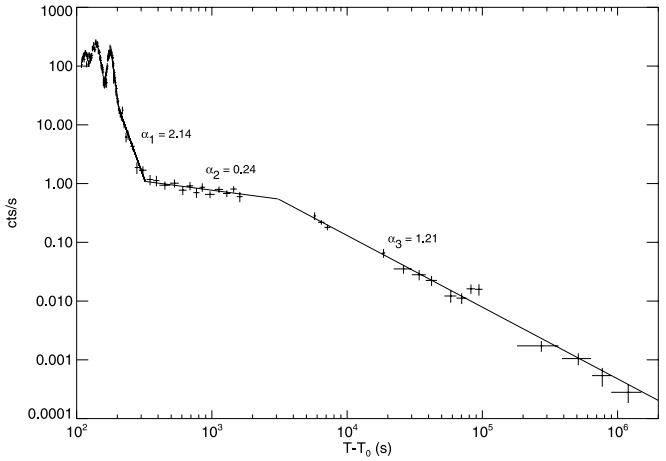

FIG. 3.—XRT light curve showing the early-time flares and three episodes of smoothly decaying afterglow emission.

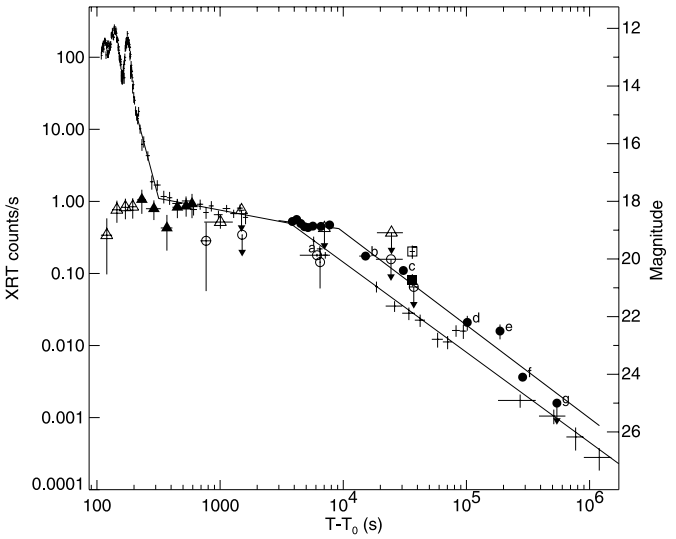

FIG. 4.—Optical measurements (*various symbols*; right-hand scale) and X-ray count rate (*plus signs*; left-hand scale) for the late-time observations. The fits to the data discussed in the text are shown as solid lines. The optical symbols are defined as follows: *filled triangles*, *V* band; *open triangles*, white; *open circles*, *B* band; *filled circles*, *R* band; *open square*, *J* band; *filled square*, *I* band. References.—*I* and *J* band: Cobb (2006); unlabled *R* band: Asfandyarof et al. (2006); labeled points: (*a*) Asfandyarof et al. (2006), (*b*) Pavlenko et al. (2006a), (*c*) Jakobsson et al. (2006b), (*d*) Pavlenko et al. (2006b), (*e*) Rumyantsev et al. (2006), (*f*) Jakobsson et al. (2006c), (*g*) Jakobsson et al. (2006d). All other points are UVOT measurements. *U*- and UVW1-band upper limits are omitted for clarity. All upper limits are 2 σ.

$\alpha_1 = 2.14 \pm 0.13$, followed by a much shallower decay starting at $t_{\rm br,1} \approx 330$ s, which is probably the afterglow emission. The afterglow decay from $T_0 + 324$ s to +1.2 Ms can be fit with a broken power-law with an initial decay slope of $\alpha_2 = 0.24 \pm 0.03$, a break at $t_{\rm br,2} = 3.2^{+1.2}_{-0.7}$ ks, and a postbreak slope of $\alpha_3 = 1.22 \pm 0.03$ (we use here the notation of Nousek et al. 2006).

A power-law fit to the 0.3–10 keV spectrum from $T_0 + 107$ s to +248 s (WT mode) gives a photon index of $\Gamma = 2.05 \pm 0.06$ and a column density of $(2.26 \pm 0.20) \times 10^{21}$ cm^{-2}. The Galactic hydrogen column density in the direction of the burst is 6.7×10^{20} cm^{-2}. An extrapolation backward in time of the flat afterglow component (α_2 segment in Fig. 3) tells us that the contribution of the underlying afterglow during this period is negligible and can safely be ignored in the spectral analysis. We also fit an absorbed single power-law model to the XRT 0.3–10 keV spectrum in PC mode (from $T_0 + 249$ s to +1610 s). Here we found a photon index of $\Gamma = 2.2 \pm 0.2$ and a column density of $(1.7 \pm 0.5) \times 10^{21}$ cm^{-2}. At later times, from $T_0 + 6096$ s to +45,416 s, the X-ray spectrum was well described by a single power-law model with photon index $\Gamma = 2.4 \pm 0.4$ and an absorbing column density of $(1.9 \pm 0.8) \times 10^{21}$ cm^{-2}.

2.3. *Swift UVOT*

The *Swift* Ultraviolet/Optical Telescope (UVOT; Roming et al. 2005) began observing the field of GRB 060714 at $T_0 + 90$ s in the settling mode and obtained the first detection in the white filter (160–650 nm) in the exposure starting at $T_0 + 108$ s (Boyd & Marshall 2006). The position of the afterglow measured in the image from the initial exposure with the white filter is R.A. = $15^{\rm h}11^{\rm m}26.444^{\rm s}$ (227.8602°), decl. = $-6°33'58.35''$ ($-6.5662°$) (J2000.0). The uncertainty of this position is likely to be dominated by systematic errors, which we estimate to be $\sim 0.5''$ (90% confidence radius) based on residuals when matching UVOT sources in the image to stars in the USNO B1.0 catalog (Monet et al. 2003). UVOT used the standard sequence of exposures for observing gamma-ray bursts. The sequence cycles through all seven lenticular filters with increasing exposure times as the time from the trigger increases. The afterglow was strongly detected in the white and *V* filters and weakly detected in the *B* filter. Figure 4 shows the UVOT detections and upper limits in the white, *V*, and *B* bands, using UVOT CALDB version 20061116 and correcting for galactic extinction using the extinction curve of Pei (1992) and the reddening from Schlegel et al. (1998). The count rates in the white filter were converted to equivalent *V* magnitudes using the ratio of the average count rates in white and *V* seen in the multiple exposures between $T_0 + 700$ s and +1582 s. Upper limits (2 σ) in the *U* and UVW1 bands (omitted for clarity from Fig. 4) are $U > 18.6$ (667 s $< T_0 <$ 835 s), and UVW1 > 19.3 (643 s $< T_0 <$ 811 s). This lack of detection is consistent with the reported burst redshift of $z = 2.71$ (Jakobsson et al. 2006a; see § 2.4) which shifts the Lyman edge to 338 nm, cutting out much of the *U* and all of the UVW1 band. The Lyman forest is also likely to reduce the flux in the *U* and *B* filters.

During the time period in which the X-ray light curve is showing flares followed by a steep decline, the optical light curve in the *V* band is essentially flat and at the same level as the afterglow. This tells us that the flaring activity does not manifest itself in the optical and suggests that the afterglow component dominates the optical light curve even at early times. This is consistent with what has been seen for other bursts with intense early flaring activity (for example Romano et al. 2006; Guetta et al. 2007), and for the unusual "late plateau" of GRB 070110 (Troja et al. 2007). At least during the time for which we have optical data, this burst seems to behave in a similar way to GRB 050401 (Rykoff et al. 2005) in which the optical and X-ray emission vary independently, but the prompt optical emission is consistent with a backward extrapolation of the later afterglow emission.

2.4. *Other Observations*

GRB 060714 was well observed by a large number of other telescopes with detections beginning at $T_0 + 3860$ s (Asfandyarof et al. 2006) and continuing until $T_0 + 3.31$ days (Jakobsson et al. 2006c). A 2 σ upper limit of $R > 25.0$ was obtained at $T_0 +$ 6.28 days (Jakobsson et al. 2006d). Figure 4 shows the reported optical detections compared to the X-ray data. During an observation beginning 12 hr after the burst, with the FOcal Reducer and low dispersion Spectrograph for the Very Large Telescope of the European Southern Observatory, Jakobsson et al. (2006a) acquired a spectrum showing numerous absorption features which

TABLE 1
DATA DISPLAYED IN THE TOP THREE PANELS OF FIG. 5

Time Interval	Fluence (0.3–10 keV)	Fluence (15–150 keV)	E_{pk} (keV)	Power-Law Index	E_{iso} (10^{52} ergs)
−13.4–18.0	...	$3.95^{+0.45}_{-0.89}$	>77.6	1.61 ± 0.13	>3.74
70.21–86.2	...	$3.44^{+0.35}_{-2.45}$	55.5 ± 11.5	1.00 ± 0.51	$1.36^{+0.55}_{-0.29}$
86.2–102.88	...	$1.90^{+1.68}_{-0.49}$	45.0 ± 9.6	1.38 ± 0.36	$1.76^{+0.74}_{-0.39}$
107.0–121.04	1.35± 0.16	0.66 ± 0.15	9.8 ± 1.5	1.50 ± 0.16	0.64 ± 0.07
121.04–159.21	$0.58^{+0.06}_{-0.07}$	$0.06^{+0.06}_{-0.04}$	3.9 ± 0.77	1.51 ± 0.24	0.58 ± 0.10
159.21–199.21	$0.32^{+0.34}_{-0.09}$	<0.0504	0.5 ± 0.50	1.90 ± 0.26	0.36 ±0.07

NOTE.—Fluence is in units 10^{-8} erg cm^{-2}.

correspond to a redshift of $z = 2.711 \pm 0.001$ and a neutral hydrogen column density of $(6.3 \pm 1.5) \times 10^{21}$ cm^{-2}. As seen in Figure 4, the *R*-band optical light curve can be well fit to a broken power-law decay with an index $\alpha_{R,2} = 0.23 \pm 0.13$ before $T_0 + \sim 10^4$ s, and $\alpha_{R,3} = 1.29 \pm 0.10$ after. These values are very similar to the decay constants for the X-ray afterglow, $\alpha_{X,2} = 0.24 \pm 0.03$ and $\alpha_{X,3} = 1.22 \pm 0.03$, respectively. However, the break in the X-ray light curve occurs at least 3 ks (corresponding to a factor of ~2 in time) earlier than the break in the *R*-band light curve.

3. SPECTROSCOPY AND LIGHT CURVES OF THE FLARES

There were a total of five flares detected in this burst, as seen in Figure 2. The first two were seen only in the BAT; the first was during the slew and the second during times when the XRT was observing in Imaging and Photodiode mode and no detailed spectral or temporal information is available. The third one was significant in both BAT and XRT and the fourth and fifth were seen as strong flares in the XRT, and weakly in the BAT.

In the observer frame the flares lasted from ~84 to ~210 s after the onset of burst emission (at $T - 13.4$ s). Given the burst redshift of $z = 2.71$ (a quite typical value for *Swift*), in the source frame the flares extend from ~23 to ~56 s after the start of emission. Although this means that the flares are relatively early as seen in the source frame, the timing of flares varies widely in the cosmological frame of GRBs, and there is no indication that absolute timing is a distinguishing characteristic of flares. Although the timing analysis described in § 3.1 and discussed in § 4 is done in the observer frame, the conclusions are all based on relative timing and do not depend on the cosmological frame chosen.

3.1. *Spectroscopy*

All five flares were fit with a spectral model of a power law with exponential cutoff: $F(E) = A(E/100\ \mathrm{keV})^{-\alpha} \exp[-E(2 - \alpha)/E_{pk}]$, where E is the photon energy, E_{pk} is the peak energy of the $\nu F(\nu)$ spectrum, α is the photon index, and A is a normalization factor. The first two were fit to BAT alone, the last three to BAT jointly with XRT. For the fourth and fifth flares inclusion of the BAT data did not significantly affect the fit. The bars at the bottom of Figure 2 indicate the time segments used to fit each of the flares. The results of the spectral fits are shown in Table 1 and in the top two panels of Figure 5. Although there is no evidence for a smooth power-law decay underlying the flares, it is possible that they overlap each other temporally. We have increased the error bars on the flux and E_{iso} values in Table 1 to account for this overlap by extrapolating the power-law fits (§ 3.2) to each flare down to zero and estimating the fraction of the flux falling outside of the nominal start and stop times of the flare (for the upper limit), and the flux possibly due to neighboring flares (for the lower limit).

In the fits to the last three flares an absorption component was included in the model. The column densities were found to be (units 10^{21} cm^{-2}), respectively for flares 3–5, 1.91 ± 0.43, 1.86 ± 0.36, and 1.67 ± 0.22, consistent within errors to a constant value.

One can see in Figure 5 that the peak energies of the flares decrease with time and the power-law indices show a general softening of the spectra. Furthermore, the apparent linearity of the plots indicates a connection (or at least a clear trend) between the five flaring events. The time dependence of E_{pk} is well fit by a power law, with index -5.81 ± 0.68. Similarly, the time dependence of the power-law index can be fit to a power law with index 0.67 ± 0.15.

Using the redshift $z = 2.71$ for this burst, we extrapolate the total isotropic equivalent radiated energy, $E_{\gamma,iso}$ (in ergs) in the range of $1–10^4$ keV, using the definition of Amati et al. (2002). For the flares, the extrapolation fixes the E_{pk} and α values derived from the cutoff power-law fits, and uses a fixed high-energy index $\beta = -10.0$. For the prompt emission we derive a lower limit to $E_{\gamma,iso}$ from the lower limit to E_{pk}. The third panel of Figure 5 shows $E_{\gamma,iso}$ as a function of time. There is a general trend toward lower total energy output of successive flares. Here a fit to a temporal decay power law gives an index of -1.72 ± 0.46. In Figure 6 we plot E_{pk} against $E_{\gamma,iso}$ for the flares and the prompt emission. This enables us to compare the episodes of GRB 060714 to the E_{pk}-$E_{\gamma,iso}$ relationships found by Amati et al. (2002) and parameterized by Ghirlanda et al. (2004).[7] The prompt emission and the first two flares fall on or very close to the relationships, while the last three flares fall well below them. This shows that E_{pk} is falling with time more rapidly than the square of the total isotropic equivalent energy emitted in the flares, $\left(E_{\gamma,iso}\right)^2$.

3.2. *Temporal Analysis*

In addition to the spectral properties of the flares, the temporal properties can also help to tell us whether or not these events arise in the external shock (i.e., are afterglow emission).

In order to study the fine time structure of subpeaks within the flares, we have derived a robust method for distinguishing between a significant change in slope of the light curve (indicating the start or end of a new subpeak) and a statistical fluctuation. Using one-second binned light curves for both the BAT and XRT data, we applied an iterative method to find each significant episode (subpeak) during the times of the flares. In the first iteration,

[7] Since we do not see a jet break in the light curve, we are unable to constrain the $E_{pk} - E_\gamma(\theta)$ relation of Ghirlanda et al. (2004).

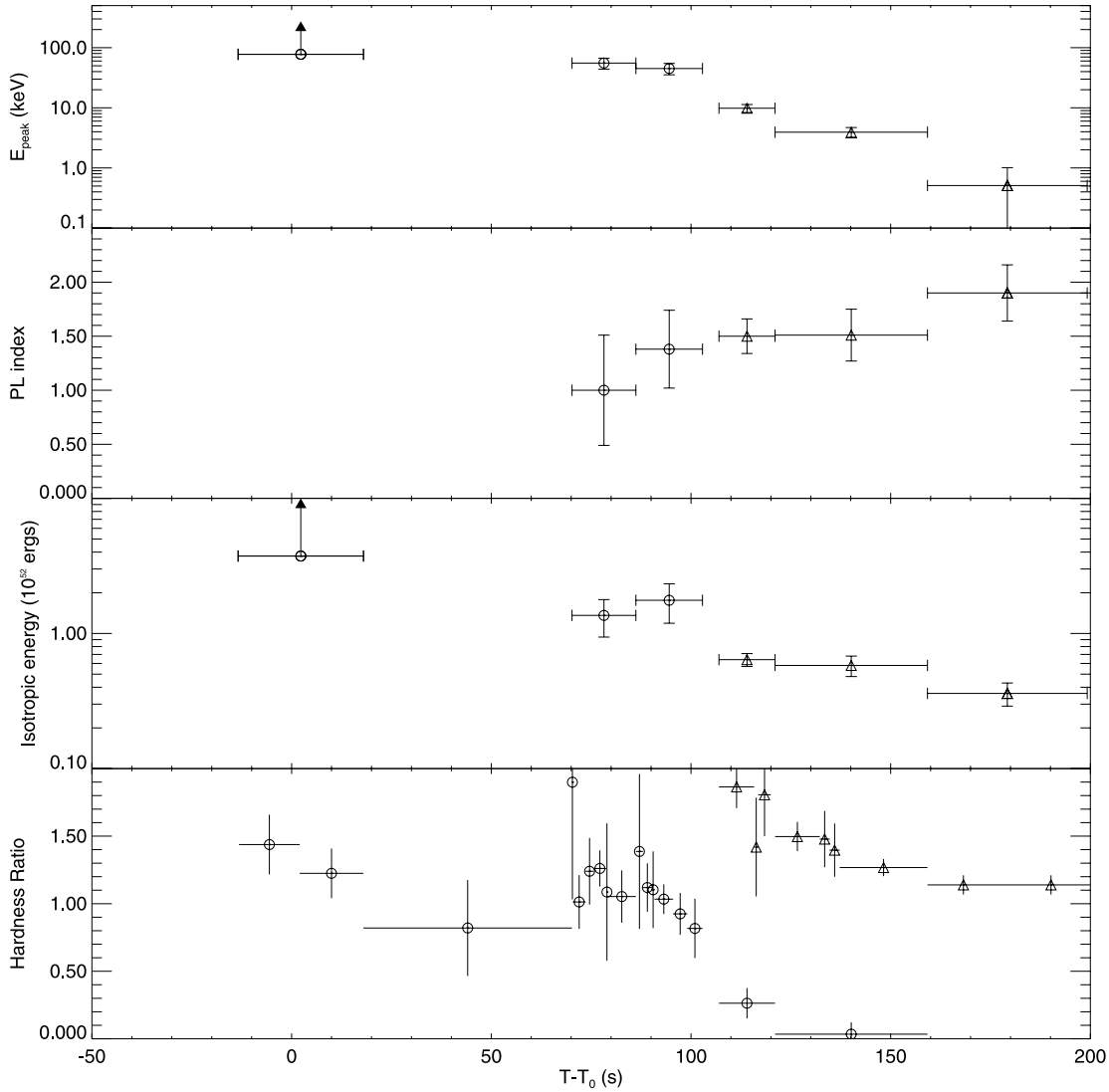

FIG. 5.—Evolution of spectral fit and energetic properties of the flares. The fits are to BAT alone (*circles*) and BAT and XRT jointly (*triangles*). We were unable to fit a cutoff power law to the prompt emission, so the points for the prompt emission show lower limits on $E_{\rm pk}$ and $E_{\rm iso}$. The top panel shows how $E_{\rm pk}$ (shown in the observer frame) changes from the prompt emission through the five flares. The second panel shows the evolution of the power-law index (α in the cutoff power-law fit) across the flares. Both of the two top plots clearly show a hard-to-soft spectral evolution as the flares progress. The third panel shows the time evolution of the isotropic radiated energy over the $1–10^4$ keV energy range, indicating the flares become progressively less energetic. The data plotted in the top three panels is also given in Table 1. The bottom panel shows hardness ratios for the burst. For the prompt emission and the first four flares the flux ratio $S(50–100\ {\rm keV})/S(25–50\ {\rm keV})$ is shown as circles. (The hardness ratio for the last flare is consistent with zero.) For the last three flares, we also show the flux ratio $S(1.5–10\ {\rm keV})/S(0.3–1.5\ {\rm keV})$ (*triangles*).

peaks were defined as local maxima (points higher than each of their nearest neighbor points) and valleys as local minima. In successive iterations we culled the peaks by requiring that a significant peak be at least three standard deviations above the valleys on either side. By this method, each point in the light curve was assigned a specific interval, either to the rise or fall of a peak, or to the periods of slow rise ($T < -13.4$ s) or slow decay (18.0 s $< T <$ 70.2 s or $T >$ 105.4 s for BAT; and $T >$ 195.6 s for XRT). We then fit each interval to a power law, $\log(R)$ versus $\log(t)$, where R is the count rate for either BAT or XRT (depending on which flare is being analyzed) and t is the time since the burst trigger. Finally, we use these power-law fits to define the actual start, apex, and end of each subpeak (not restricted to light curve bin edges). The start of each episode (t_1) is defined as the time at which the rising power-law segment of a peak crosses the falling power-law segment of either the preceding smooth decay or the previous peak. Similarly, the peak time of each interval (t_2) is the time at which the rising power-law segment of a peak meets the falling power law of the same peak. The rise time (Δt) is thus defined as $\Delta t \equiv t_2 - t_1$, while the time associated with each rise episode is $t \equiv (t_2 + t_1)/2$. Thus,

$$\frac{\Delta t}{t} \equiv \frac{2(t_2 - t_1)}{(t_2 + t_1)} = \frac{\Delta t}{(t_1 + \Delta t/2)} = \frac{\Delta t}{(t_2 - \Delta t/2)}. \quad (2)$$

The conclusions drawn in § 4 do not depend critically on the exact definitions of t or Δt.

The episodes so defined are shown graphically in Figure 7 and their main temporal properties in Table 2. The temporal decay indices are derived in two ways, detailed in the table caption. The decay index is first calculated using the burst trigger time T_0 as the reference time ($\alpha_{\rm A}$), which is the standard way that GRB

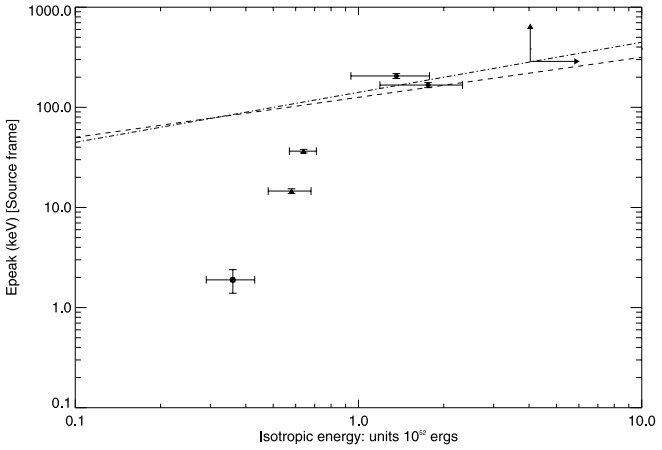

FIG. 6.—Peak energy vs. isotropic energy over the $1-10^4$ keV energy range (the same energy range used by Amati et al. 2002). The dashed line is the fit to $E_{\rm pk}$-$E_{\rm iso}$ derived by Ghirlanda et al. (2004) and the dot-dashed line is the fit derived by Amati et al. (2002). The time ordering of the flares goes monotonically from highest $E_{\rm pk}$ to lowest. The prompt emission and the first two flares detected fall on the Amati relation while the last three flares fall below.

decay indexes are calculated, and would be appropriate for the flares if they were afterglow emission. However, since the resulting values of the decay index $\alpha_{\rm A}$ are very high, corresponding to a very steep decay which is very hard to produce by the afterglow emission (Kumar & Panaitescu 2000; Nakar & Piran 2003), we also want to explore the possibility that the flares arise from late-time sporadic activity of the central source. In this case the appropriate reference time, t_0, would roughly correspond to the onset of the individual flare or subflare whose decay rate we wish to quantify ($\alpha_{\rm B}$). Both decay indices are shown in Table 2, although values quoted in Figure 3 are taken as the decay index $\alpha_{\rm B}$. Even taking the second definition, $\alpha_{\rm B}$, the decay indexes of the flares are all very steep, and except for flare 4, much steeper than either the decay of the emission just before the first flare ($\alpha = 1.16 \pm 0.47$) or the decay immediately after the fifth flare ($\alpha = 2.14 \pm 0.13$). The decay slope immediately after the last flare is still much steeper than the afterglow beginning at $T+ \sim 320$ s, so it is likely part of the prompt emission as well. We note, however, that $\alpha_{\rm B}$ does not exceed $2 + \beta$ [within the statistical uncertainty, where $F_\nu \propto \nu^{-\beta}(t - t_0)^{-\alpha}$], which is the steepest decay allowed by the "high-latitude" emission (Kumar & Panaitescu 2000), and thus the

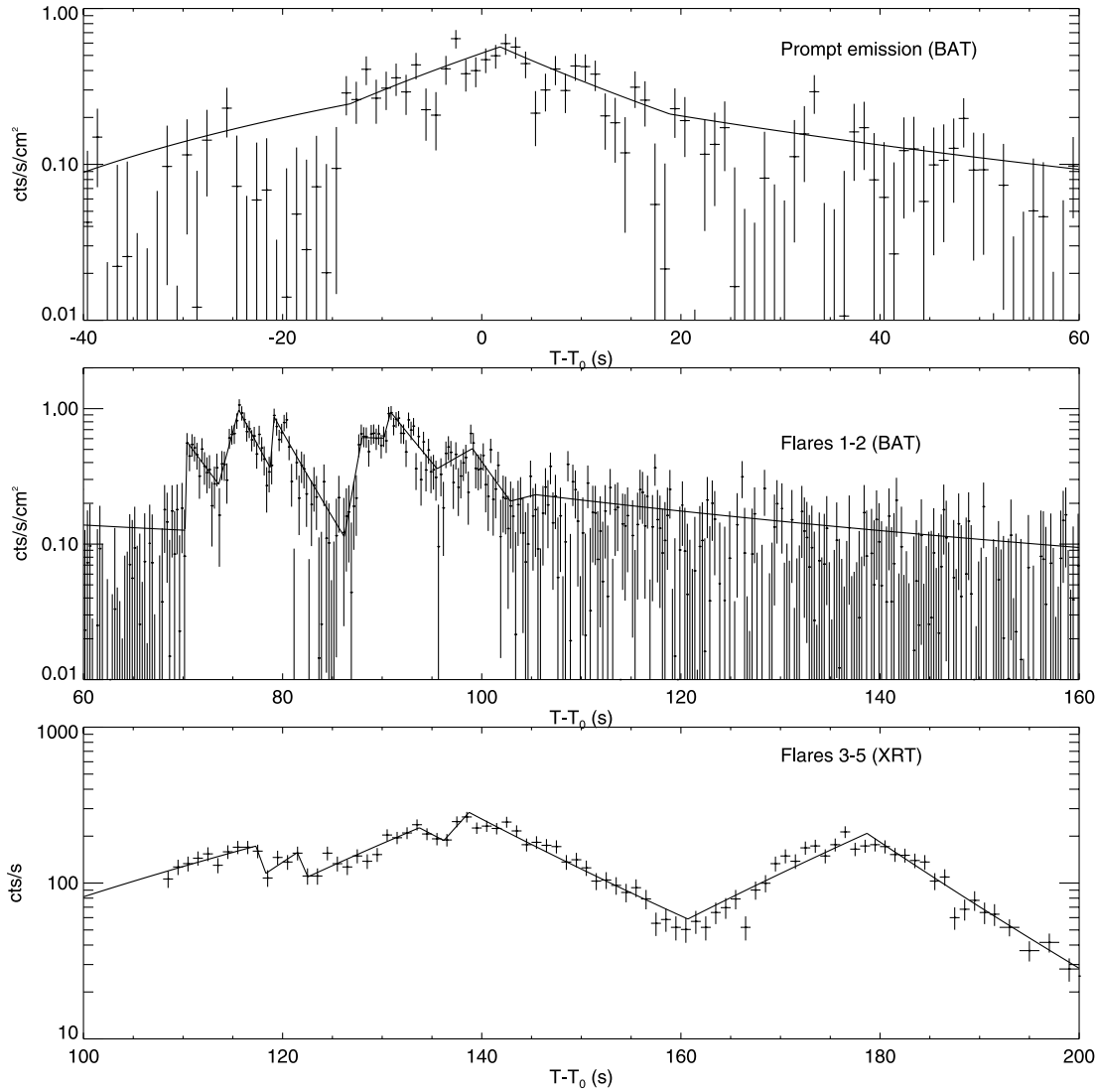

FIG. 7.—Prompt emission (*top*), BAT-detected flares (*middle*), and XRT-detected flares (*bottom*), all on the same timescale. The solid lines on the plot show the best power-law fit to each individual segment of the light curve, and the changes in slope indicate the start, apex, and end of each subpeak. The method for defining the intervals is given in the text, and decay constants are listed in Table 2. One can note the sharp temporal features (subpeaks) of the flares. It is also clear that the X-ray flares are longer than the BAT flares, a feature also seen in Romano et al. (2006) and consistent with previous results showing that the duration of pulses in prompt emission are longer at low energy than at high energy.

TABLE 2
Temporal Decay Slopes of Flares

Flare (1)	Peak (2)	Start t_1 (3)	Rise Time Δt (s) (4)	Decay Index α_A (5)	t_0 for α_B (s) (6)	Decay Index α_B (7)
Prompt	...	−13.4	15.5	5.4 ± 1.1	−13.17	2.34 ± 0.45
Prompt decay	...	18.0	...	2.1 ± 0.8	−13.17	1.16 ± 0.47
1	1	70.2	0.19	16.3 ± 5.3	70.21	0.29 ± 0.11
1	2	73.6	2.01	24.0 ± 4.1	70.21	2.14 ± 0.36
1	3	78.8	0.39	23.9 ± 2.8	70.21	3.35 ± 0.39
2	1	86.2	1.77	19.2 ± 2.5	86.2	1.33 ± 0.18
2	2	95.5	3.54	23.7 ± 4.8	86.2	3.50 ± 0.71
3	1	102.9	2.54	46.9 ± 17.7	108.5	3.77 ± 1.42
3	2	118.3	3.14	41.2 ± 18.2	108.5	4.56 ± 2.01
4	1	122.5	11.2	10.3 ± 5.1	122.54	0.96 ± 0.46
4	2	136.2	2.52	10.7 ± 0.5	122.54	1.78 ± 0.08
5	...	160.7	18.0	17.7 ± 0.7	160.71	2.73 ± 0.12
Final prompt decay	...	195.6	...	6.34 ± 0.39	160.71	2.14 ± 0.13
Shallow afterglow	...	323.8	...	0.31 ± 0.17	160.71	0.24 ± 0.03
Steep afterglow	...	3200	...	1.24 ± 0.05	160.71	1.21 ± 0.03

Notes.—Flares are numbered as in the text and Figs. 1 and 2. Times are with reference to the trigger time T_0, and the definition of the rise time is given in the text. The decay index is derived through a fit to $R \propto (t - t_0)^{-\alpha}$, where R is the photon event rate, t is the time, and t_0 is defined as the trigger time T_0 when deriving α_A (col. [5]), and as the start of the particular peak or flare when deriving α_B (col. [7]). The values of t_0 used in the derivation of α_B are shown in column (6).

decay of the flares and subflares is consistent with the expectations for late-time intermittent activity of the central source.

4. DISCUSSION

4.1. *The External Shock*

The temporal properties of the flares provide strong evidence against an external shock (i.e., afterglow) origin for them. Figure 8 shows the fractional increase in flux, $\Delta F/F$, versus the ratio of the rise time (Δt) to the peak of each flare or subflare and the time (t) from the GRB trigger, $\Delta t/t$ (see eq. [2]). It can clearly be seen that large amplitude variations in the flux, $\Delta F/F \gtrsim 1$, occur on very short timescales, $\Delta t/t \ll 1$. This basically rules out an external shock origin for the flares (see, e.g., Ioka et al. 2005; Nakar 2006; Lazzati & Perna 2007). We also note that the flares are very different from the smooth, late-time tail emission in the 20–100 keV band which was observed to follow many of the bursts detected by the Burst and Transient Source Experiment (BATSE; Connaughton 2002). The tail emission is temporally much smoother than the flares of GRB 060714 and at a much lower level (as a ratio to the peak of the prompt emission). Also, Giblin et al. (2002) identify a subset of the BATSE bursts that have high-energy decay emission consistent with forward external shocks. Although it is below detectability for BAT, it is possible that the tail emission is seen after the last flare in the $\alpha_1 = 2.14$ decay segment (Fig. 3). This decay index is consistent with the average temporal decay index reported for BATSE tail emission, -2.03 ± 0.51 (Giblin et al. 2002).

The major possible sources of variability in the afterglow light curves (i.e., in the emission from the external shock) are (1) a variable external density (Wang & Loeb 2000; Lazzati et al. 2002; Nakar et al. 2003), (2) a "patchy shell," i.e., angular inhomogeneity within the outflow (Kumar & Piran 2000b; Nakar et al. 2003), and (3) "refreshed shocks," i.e., relatively slow shells that were ejected from the central source toward the end of the prompt emission and catch up with the afterglow shock as the latter decelerates to a Lorentz factor slightly lower than that of the shells (Rees & Mészáros 1998; Kumar & Piran 2000a). Such a sharp ($\Delta t/t \ll 1$) large amplitude ($\Delta F/F \gtrsim 1$) rise in the observed flux, as we find for GRB 060714 (see Fig. 8), cannot be caused by a sudden increase in the external density (Nakar & Granot 2006). In addition, a "patchy shell" produces $\Delta t/t \sim 1$ (Nakar & Oren 2004) and cannot account for the observed $\Delta t/t \ll 1$, since new "bright spots" in the outflow become visible (i.e., enter the observed region of angle $\sim 1/\gamma$ around the line of sight) gradually, on the dynamical time ($\Delta t \sim t$). Finally, "refreshed shocks" produce $\Delta t/t \sim 1$ before the jet break time, when the rise time Δt is dominated by the angular time $t_\theta \approx R/2c\gamma^2$. After the jet break time, the angular

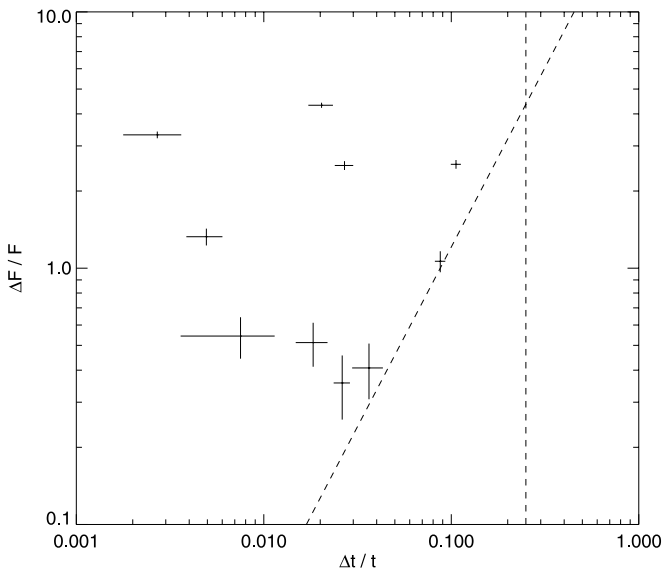

Fig. 8.—Plot of $\Delta t/t$ vs. $\Delta F/F$. The flux ratio $\Delta F/F$ is derived as $\Delta F = [F(t_2) - F(t_1)]$ and $F = F(t_1)$, where $F(t_1)$ and $F(t_2)$ are the flux at the start and top of each peak, respectively. In this notation $\Delta F/F = 1$ means a doubling of the flux. This figure shows that for all peaks $\Delta F/F \sim 1$ while $\Delta t/t \ll 1$. The area to the right of the dashed lines indicates the kinematically allowed region for afterglow variability derived by Ioka et al. (2005). The vertical line indicates that refreshed shocks cannot make a bump with $\Delta t < t/4$. Ioka et al. (2005) also argue that ambient density fluctuations cannot make a bump in afterglow light curves larger than the limit indicated by the diagonal line.

the ratio of electromagnetic to kinetic energies of the outflow, and primed quantities are measured in the comoving frame. The relative velocity between the two shells is

$$\beta_{21} = \frac{\beta_2 - \beta_1}{1 - \beta_2\beta_1} \cong \frac{\gamma_2^2 - \gamma_1^2}{\gamma_2^2 + \gamma_1^2} \approx \frac{\Delta\gamma}{\gamma} \ll 1. \tag{A4}$$

Thus, the shocks going into the two colliding shells are Newtonian for $\Delta\gamma/\gamma \ll 1$, and the compression ratio is $\rho'_{\rm ps}/\rho' \approx 4$, where the subscript "ps" is for "postshock." For equal density shells, the relative velocity of the upstream and downstream fluids is $\beta_{\rm ud} \approx \beta_{21}/2 \approx \Delta\gamma/2\gamma$, and the internal energy per unit rest-energy is[8] $e'_{\rm ps}/\rho'_{\rm ps}c^2 \approx \beta_{\rm ud}^2/2 \approx (\Delta\gamma/\gamma)^2/8$. Thus, the minimal random Lorentz factor of the power-law distribution of relativistic electrons scales as

$$\gamma_m \propto \epsilon_e \frac{e'_{\rm ps}}{\rho'_{\rm ps}} \propto \epsilon_e \left(\frac{\Delta\gamma}{\gamma}\right)^2, \tag{A5}$$

where ϵ_e is the fraction of the postshock internal energy that goes into such a population of relativistic electrons. The internal energy in the shocked regions scales as

$$e'_{\rm ps} \sim \frac{1}{8}\left(\frac{\Delta\gamma}{\gamma}\right)^2 \rho' c^2 \propto \left(\frac{\Delta\gamma}{\gamma}\right)^2 \frac{L_{\rm iso}}{\gamma^2 R^2} \propto \left(\frac{\Delta\gamma}{\gamma}\right)^4 \frac{L_{\rm iso}}{\gamma^6 \left(\Delta t_{\rm ej}\right)^2}, \tag{A6}$$

where we evaluate the values of the relevant quantities at $R \approx R_{\rm IS}$, using equation (A1).

If the magnetic field holds a constant fraction, ϵ_B, of the internal energy behind the shock, as is often assumed for a shock-generated magnetic field, then such an equipartition field[9] would scale as

$$B'_{\rm eq} \propto \left(\epsilon_B e'_{\rm ps}\right)^{1/2} \propto \epsilon_B^{1/2}\left(\frac{\Delta\gamma}{\gamma}\right)^2 L_{\rm iso}^{1/2}\gamma^{-3}\left(\Delta t_{\rm ej}\right)^{-1}. \tag{A7}$$

However, some magnetic field is expected to be advected with the outflow from the central source. At large distances form the source such a field is expected to be primarily in the tangential direction (normal to the radial direction), so that it would be amplified in the shock by the compression ratio, $B'_{\rm adv,ps} \approx 4B'_{\rm adv}$, where $(B'_{\rm adv})^2 = 4\pi\rho' c^2\sigma$. Thus, for equal mass shells the ratio of the magnetic energy density associated with this field to the internal energy density in the shocked region is $(B'_{\rm adv,ps})^2/8\pi e'_{\rm ps} \approx 64\sigma(\Delta\gamma/\gamma)^{-2}$, so that the shock compressed advected field would typically exceed an equipartition shock generated field for reasonable values of σ, i.e., $\sigma \gtrsim 10^{-3}(\Delta\gamma/\gamma)^2(\epsilon_B/0.1)$. In this case $B'_{\rm ps} \approx B'_{\rm adv,ps}$, where

$$B'_{\rm adv,ps} \approx 8c\sqrt{\pi\rho'\sigma} \propto \sigma^{1/2}\left(\frac{\Delta\gamma}{\gamma}\right) L_{\rm iso}^{1/2}\gamma^{-3}\left(\Delta t_{\rm ej}\right)^{-1}. \tag{A8}$$

The synchrotron frequency of the electrons with the minimal random Lorentz factor, γ_m, scales as

$$\nu_m \approx \gamma \frac{eB'_{\rm ps}\gamma_m^2}{2\pi m_e c} \propto \begin{cases} \epsilon_B^{1/2}\left(\dfrac{\Delta\gamma}{\gamma}\right)^6 \epsilon_e^2 L_{\rm iso}^{1/2}\gamma^{-2}\left(\Delta t_{\rm ej}\right)^{-1} & \text{for equipartition,} \\ \sigma^{1/2}\left(\dfrac{\Delta\gamma}{\gamma}\right)^5 \epsilon_e^2 L_{\rm iso}^{1/2}\gamma^{-2}\left(\Delta t_{\rm ej}\right)^{-1} & \text{for an advected field.} \end{cases} \tag{A9}$$

The random Lorentz factor of electrons that cool on the dynamical time (shell crossing time), $t' \sim R_{\rm IS}/\gamma$, scales as

$$\gamma_c \approx \frac{6\pi m_e c}{\sigma_{\rm T}\left(B'_{\rm ps}\right)^2 (R_{\rm IS}/\gamma)(1+Y)} \propto \begin{cases} (1+Y)^{-1}\epsilon_B^{-1}\left(\dfrac{\Delta\gamma}{\gamma}\right)^{-3} L_{\rm iso}^{-1}\gamma^5\Delta t_{\rm ej} & \text{for equipartition,} \\ (1+Y)^{-1}\sigma^{-1}\left(\dfrac{\Delta\gamma}{\gamma}\right)^{-1} L_{\rm iso}^{-1}\gamma^5\Delta t_{\rm ej} & \text{for an advected field,} \end{cases} \tag{A10}$$

where Y is the Compton y-parameter.

The factor of $(1+Y)$ can be safely dropped from the expression for the advected field, since in this case $Y \ll 1$ (it is included here for completeness). This can be seen as follows. In general $Y(1+Y) \approx \beta_{2,\rm sh}\epsilon_{\rm rad}\epsilon_e/\epsilon_B$ (see, e.g., Sari & Esin 2001), where $\beta_{2,\rm sh}$ is the velocity of the downstream medium relative to the shock front, which in our case is $\beta_{2,\rm sh} \sim \beta_{21} \approx \Delta\gamma/\gamma \ll 1$, and $\epsilon_{\rm rad} \sim \min[1, (\nu_m/\nu_c)^{(p-2)/2}]$ is the fraction of the energy in the postshock power-law distribution of relativistic electrons that is radiated away. Here $\epsilon_B = (B'_{\rm ps})^2/8\pi e'_{\rm ps}$, which

[8] In this case, if the mass of the shells is also the same, the two shocks finish crossing the two shells together, and this is also the fraction ϵ of the total energy that is converted into internal energy. As shown below, for a fixed Lorentz factor contrast $\Delta\gamma/\gamma$, ϵ is maximal for equal mass shells.

[9] We use the term "equipartition field" for simplicity, even though strictly speaking it holds a constant fraction ($\epsilon_B^{1/2}$, generally smaller than unity) of the equipartition value.

for a subequipartition field is < 1, but for a field advected from the source and compressed by the shock it is (see above) $\approx 64\sigma(\Delta\gamma/\gamma)^{-2}$, which is $\gg 1$ unless the magnetization of the outflow is extremely low, $\sigma \lesssim 10^{-2}(\Delta\gamma/\gamma)^2$. Thus, $Y \sim \epsilon_e \epsilon_{\rm rad} 10^{-2}\sigma^{-1}(\Delta\gamma/\gamma)^3 \ll 1$. For a shock-generated field that is a constant fraction of equipartition Y would also be small unless $\epsilon_{\rm rad}\epsilon_e/\epsilon_B \gtrsim \gamma/\Delta\gamma$.

The cooling break frequency thus scales as

$$\nu_c \approx \gamma \frac{eB'_{\rm ps}\gamma_c^2}{2\pi m_e c} \propto \begin{cases} (1+Y)^{-2}\epsilon_B^{-3/2}\left(\dfrac{\Delta\gamma}{\gamma}\right)^{-4} L_{\rm iso}^{-3/2}\gamma^8\Delta t_{\rm ej} & \text{for equipartition,} \\ (1+Y)^{-2}\sigma^{-3/2}\left(\dfrac{\Delta\gamma}{\gamma}\right)^{-1} L_{\rm iso}^{-3/2}\gamma^8\Delta t_{\rm ej} & \text{for an advected field.} \end{cases} \tag{A11}$$

Finally, we derive the fraction, ϵ, of the total energy that is converted into internal energy during the collision between the two shells (in the limit $\sigma \ll 1$ and $\Delta\gamma/\gamma \ll 1$). Conservation of energy and momentum read

$$\gamma_1 m_1 + \gamma_2 m_2 = \gamma_f M, \tag{A12}$$

$$\gamma_1\beta_1 m_1 + \gamma_2\beta_2 m_2 = \gamma_f\beta_f M, \tag{A13}$$

where $\gamma_f = (1-\beta_f^2)^{-1/2}$ is the final Lorentz factor and $M = m_1 + m_2 + E'_{\rm int}/c^2$, where $E'_{\rm int}$ is the internal energy that was produced in the collision, as measured in the rest frame of the merged shell, while its value in the lab frame is $E_{\rm int} = \gamma_f E'_{\rm int}$. One obtains β_f from the ratio of the two equations, and for $\gamma \gg 1$ we have

$$\frac{1}{2\gamma_f^2} \cong 1 - \beta_f = \frac{\gamma_1(1-\beta_1)m_1 + \gamma_2(1-\beta_2)m_2}{\gamma_1 m_1 + \gamma_2 m_2} \cong \frac{m_1/\gamma_1 + m_2/\gamma_2}{2(\gamma_1 m_1 + \gamma_2 m_2)}, \tag{A14}$$

and therefore

$$\gamma_f \cong \sqrt{\frac{\gamma_1 m_1 + \gamma_2 m_2}{m_1/\gamma_1 + m_2/\gamma_2}}. \tag{A15}$$

Thus, we have

$$\epsilon = \frac{E_{\rm int}}{(\gamma_1 m_1 + \gamma_2 m_2)c^2} = 1 - \frac{\gamma_f(m_1+m_2)}{\gamma_1 m_1 + \gamma_2 m_2} \cong 1 - \left[1 + \frac{m_1 m_2}{(m_1+m_2)^2}\left(\frac{\gamma_2}{\gamma_1} + \frac{\gamma_1}{\gamma_2} - 2\right)\right]^{-1/2}, \tag{A16}$$

and since for $\Delta\gamma/\gamma \ll 1$ (in addition to $\gamma \gg 1$),

$$2(\gamma_{21} - 1) \cong \frac{\gamma_2}{\gamma_1} + \frac{\gamma_1}{\gamma_2} - 2 \approx \left(\frac{\Delta\gamma}{\gamma}\right)^2 \ll 1, \tag{A17}$$

then

$$\epsilon \approx \frac{m_1 m_2}{2(m_1+m_2)^2}\left(\frac{\Delta\gamma}{\gamma}\right)^2 = \frac{x}{2(1+x)^2}\left(\frac{\Delta\gamma}{\gamma}\right)^2, \tag{A18}$$

where $x = m_2/m_1$ (or alternatively m_1/m_2) is the rest-mass ratio of the two shells.

REFERENCES

Amati, L., et al. 2002, A&A, 390, 81
Asfandyarof, I., et al. 2006, GCN Circ 5434, http://gcn.gsfc.nasa.gov/gcn3/5434.gcn3
Band, D. L., & Ford, L. 1998, Adv. Space Res., 22, 1093
Barraud, C., Daigne, F., Mochkovitch, R., & Atteia, J. L. 2005, A&A, 440, 809
Barthelmy, S., et al. 2005a, Space Sci. Rev., 120, 143
Boyd, P., & Marshall, F. 2006, GCN Circ 5357, http://gcn.gsfc.nasa.gov/gcn3/5357.gcn3
Burrows, D. N., et al. 2005a, Space Sci. Rev., 120, 165
———. 2005b, Science, 309, 1833
———. 2007, Philos. Trans. R. Soc. London A, 365, 1213
Butler, N., & Kocevski, D. 2007, ApJ, in press (astro-ph/0612564)
Chincarini, G., et al. 2007, ApJ, submitted (astro-ph/0702371)
Cobb, B. E. 2006, GCN Circ 5323, http://gcn.gsfc.nasa.gov/gcn3/5323.gcn3
Connaughton, V. 2002, ApJ, 567, 1028
Falcone, A.. et al. 2006, ApJ, 641, 1010
Fan, Y. Z., & Wei, D. M. 2005, MNRAS, 364, L42
Gehrels, N., et al. 2004, ApJ, 611, 1005
Ghirlanda, G., et al. 2004, ApJ, 616, 331
Giannios, D. 2006, A&A, 455, L5
Giblin, T. W., et al. 2002, ApJ, 570, 573
Granot, J. 2007, in Rev. Mex. AA Ser. Conf., 27, 140
Granot, J., Nakar, E., & Piran, T. 2003, Nature, 426, 138
Guetta, D., et al. 2007, A&A, 461, 95
Hill, J., et al. 2004, Proc. SPIE, 5165, 217
Ioka, K., Kobayashi, S., & Zhang, B. 2005, ApJ, 631, 429
Jakobsson, P., et al. 2006a, A&A, 460, L13
———. 2006b, GCN Circ 5320, http://gcn.gsfc.nasa.gov/gcn3/5320.gcn3
———. 2006c, GCN Circ 5337, http://gcn.gsfc.nasa.gov/gcn3/5337.gcn3
———. 2006d, GCN Circ 5355, http://gcn.gsfc.nasa.gov/gcn3/5355.gcn3
Kaneko, Y., et al. 2006, ApJS, 166, 298
King, A., et al. 2005, ApJ, 630, L113

Kobayashi, S., Piran, T., & Sari, R. 1997, ApJ, 490, 92
Kocevski, D., Butler, N., & Bloom, J. S. 2007, ApJ, in press (astro-ph/0702452)
Krimm, H. A., et al. 2006a, GCN Circ 5311, http://gcn.gsfc.nasa.gov/gcn3/5311.gcn3
———. 2006b, GCN Circ 5334, http://gcn.gsfc.nasa.gov/gcn3/5334.gcn3
Kumar, P., & Panaitescu, A. 2000, ApJ, 541, L51
Kumar, P., & Piran, T. 2000a, ApJ, 532, 286
———. 2000b, ApJ, 535, 152
Lazzati, D., & Perna, R. 2007, MNRAS, 375, L46
Lazzati, D., Rossi, E., Covino, S., Ghisellini, G., & Malesani, D. 2002, A&A, 396, L5
Lyutikov, M., & Blandford, R. 2002, in Beaming and Jets in Gamma Ray Bursts, ed. R. Ouyed (eConf 0208122; Stanford: SLAC), 146
MacFadyen, A. I., Woosley, S. E., & Heger, A. 2001, ApJ, 550, 410
Monet, D. G., et al. 2003, AJ, 125, 984
Moretti, A., et al. 2005, Proc. SPIE, 5898, 360
Nakar, E. 2007, Phys. Rep., 442, 166
Nakar, E., & Granot, J. 2006, MNRAS, submitted (astro-ph/0606011)
Nakar, E., & Oren, Y. 2004, ApJ, 602, L97
Nakar, E., & Piran, T. 2002, ApJ, 572, L139
———. 2003, ApJ, 598, 400
Nakar, E., Piran, T., & Granot, J. 2003, NewA, 8, 495
Nemiroff, R. J., et al. 1994, ApJ, 423, 432
Nousek, J. A., et al. 2006, ApJ, 642, 389
O'Brien, P. T., et al. 2006, ApJ, 647, 1213
Panaitescu, A., Mészáros, P., Gehrels, N., Burrows, D., & Nousek, J. 2006, MNRAS, 366, 1357
Pavlenko, E., et al. 2006a, GCN Circ 5317, http://gcn.gsfc.nasa.gov/gcn3/5317.gcn3
———. 2006b, GCN Circ 5324, http://gcn.gsfc.nasa.gov/gcn3/5324.gcn3
Pei, Y. C. 1992, ApJ, 395, 130
Perna, R., Armitage, P., & Zhang, B. 2006, ApJ, 636, L29
Perri, M., et al. 2006, GCN Circ 5321, http://gcn.gsfc.nasa.gov/gcn3/5321.gcn3
Rees, M. J., & Mészáros, P. 1994, ApJ, 430, L93
———. 1998, ApJ, 496, L1
Romano, P., et al. 2006, A&A, 456, 917
Roming, P. W. A., et al. 2005, Space Sci. Rev., 120, 95
———. 2006, ApJ, 651, 985
Rumyantsev, V., et al. 2006, GCN Circ 5336, http://gcn.gsfc.nasa.gov/gcn3/5336.gcn3
Rykoff, E. S., et al. 2005, ApJ, 631, L121
Sakamoto, T., et al. 2006, ApJ, 636, L73
———. 2007, ApJ, submitted
Sari, R., & Esin, A. A. 2001, ApJ, 548, 787
Schlegel, D. J., Finkbeiner, D. P., & Davis, M. 1998, ApJ, 500, 525
Thompson, C. 2006, ApJ, 651, 333
Troja, E., et al. 2007, ApJ, in press (astro-ph/0702220)
Wang, X., & Loeb, A. 2000, ApJ, 535, 788
Zhang, B., et al. 2006, ApJ, 642, 354
———. 2007, ApJ, 655, L25

GRB 060714: NO CLEAR DIVIDING LINE BETWEEN PROMPT EMISSION AND X-RAY FLARES

H. A. Krimm,[1,2] J. Granot,[3] F. E. Marshall,[4] M. Perri,[5] S. D. Barthelmy,[4] D. N. Burrows,[6]
N. Gehrels,[4] P. Mészáros,[6] and D. Morris[6]

Received 2007 February 22; accepted 2007 April 20

ABSTRACT

The long gamma-ray burst GRB 060714 was observed to exhibit a series of five X-ray flares beginning 70 s after the burst trigger T_0 and continuing until $T_0 + 200$ s. The first two flares were detected by the Burst Alert Telescope (BAT) on the *Swift* satellite, before *Swift*